PAPER

Check for updates

Lipid bilayer fracture under uniaxial stretch†

Rachel Joanne Goodband [ID] ‡ and Margarita Staykova [ID] *

Most studies on pore formation in lipid membranes focus on lipid vesicles under isotropic tension. These models however fail to replicate the anisotropic stresses encountered by living cells and the complex rheological properties of the cell membrane arising from its interactions with the underlying cytoskeleton. Here, we employ a custom-built device to impose uniaxial stretch on PDMS-supported lipid membranes. We show that in contrast to the circular pores in vesicles, supported membranes under uniaxial loading open elliptical pores that are aligned perpendicularly to the direction of stretch. We discuss the constraints on tension diffusion in supported membranes, and how tension distribution determines the density and the shape of the membrane pores in relation to the applied strain rate and strain magnitude. Our paper shows for the first time that lipid membranes can exhibit a fracture behavior similar to the fracture of soft gels under tensile loading.

1. Introduction

Cell membrane rupture is a process with significant biological consequences, because it may lead to cell death. Cells that routinely experience membrane rupture include cardiac and skeletal myocytes in contracting muscles, migrating fibroblasts and dendritic cells in dense tissues, and epithelial or endothelial cells lining biological cavities.[1–3] The mechanism of membrane rupture has primarily been explored in model lipid vesicles, where an isotropic increase in membrane tension, usually by osmotic shock, leads to the formation of circular pores.[4–6] The circular shape of the membrane pores and the dynamics of membrane closure are governed by pore edge tension, membrane tension and viscosity.[4,7] Vesicle systems however do not offer a good representation of the cell membrane rupture. Firstly, anisotropic mechanical loads, which are commonly experienced by cells, cannot be replicated in vesicles. Secondly, the dynamics of pure lipid membranes differs significantly from that of the plasma cell membrane, where lipid redistribution is obstructed by immobile protein anchors and cytoskeletal adhesion.[8,9]

Membrane rupture of substrate-supported lipid bilayers (SLBs) differs significantly from that in vesicles. We argue that SLB models are a more realistic biomimetic model for studying response to tension because they capture the frictional interaction of the cell membrane to other structures (cyoskeleton, protein anchors) and reflect its obstructed dynamics. SLBs have

been successfully used to explain the formation of noncircular pores in adhering cells.[10] When spreading on solid substrates with low density of pinning points, both cellular and artifical membranes develop floral pores due to growing membrane fingering instabilities.[10–13] In contrast, spreading on substrates with high pinning points density induces a fractal membrane rupture behviour, consistent with invasion percolation in disordered media.[10,12]

In this work, we set out to explore the fracture behavior of lipid membranes under anisotropic stretch. We take advantage of our previous work on coupling membranes to deformable polydimethylsiloxane (PDMS) which have examined the membrane area regulation under stretch and compression.[14,15] Here we develop a simple PDMS stretching device that can deliver uni-directional stretch on SLBs. To our surprise, we find that SLBs open elliptical pores oriented perpendicularly to the stretch direction, contrasting with simulations that predict circular pores in unsupported membranes under uniaxial stretch.[16,17] These elliptical pores suggest a previously undiscussed analogy between membrane poration and the fracture mechanisms of soft gels under tensile loading.

2. Materials and methods

2.1. Consumables

1,2-Dioleoyl-*sn*-glycero-3-phosphocholine (DOPC) and 1,2-dipalmitoyl-*sn*-glycero-3-phosphoethanolamine-*N*-(lissamine rhodamine B sulfonyl) (ammonium salt) (Rh-DPPE) were purchased from Avanti Polar Lipids (Alabaster, AL) and used without further purification. Chloroform, trizma buffer, and sucrose were purchased from Sigma Aldrich. Polydimethylsiloxane (PDMS), curing agent

Department of Physics, Durham University, South Rd, DH1 3LE, Durham, UK.
E-mail: margarita.staykova@durham.ac.uk
† Electronic supplementary information (ESI) available. See DOI: **https://doi.org/10.1039/d4sm01410c**
‡ Present address: Department of Mechanical and Manufacturing Engineering, School of Engineering, Trinity College Dublin, Ireland. E-mail: goodbanr@tcd.ie

(Sylgard 184 Silicone Elastomer Kit, catalog no. 240401 9862), microscope slides and cover glasses from VWR (catalog no. 48366 045) were used.

2.2. Membrane stretching device

To stretch the supported lipid bilayers, we use a custom-made PDMS device as shown in Fig. 1a. A fixed amount of PDMS polymer melt, mixed with curing agent in 10 : 1 ratio is poured in a petridishes to create PDMS sheets of certain thickness, 5 mm and 100 μm in our case, and baked for 12 h to complete the crosslinking process. The base of the device is a 2 cm × 2 cm × 5 mm PDMS slab with a 8 mm diameter hole in the middle, bonded to a microscope slide on one side (i). The bonding is achieved by plasma oxidising both surfaces for 20 s (Tantec VacuLAB plasma chamber at 300 W, 1 mbar air), bringing them in contact and leaving them for 20 min on a hot plate. We insert a rectangular acrylic ridge that is 1 mm wide, 8 mm long (precisely the diameter of the hole), 5 mm high (precisely the thickness of the PDMS slab) (ii). We seal then the upper side of the PDMS slab with 100 μm PDMS sheet using plasma treatment to achieve permanent bonding (iii). The contact between the PDMS sheet and the acrylic ridge is lubricated using a small amount of silicone grease. The so-formed cavity is then connected to a syringe pump *via* a small side opening. The gradual withdrawal of air from the chamber exerts a suction force on the PDMS sheet, whose freestanding surface is deformed inwards, and the region supported by the acrylic piece is uni-directionally stretched in direction orthogonal to the ridge's long axis (Fig. 1a, side and top views). The rate and the final withdrawal volume of the pump set the strain rate and magnitude, respectively. The device can easily be reconfigured for biaxial stretch by replacing the rectangular acrylic post Fig. 1a(ii) with a circular one.

2.3. Supported lipid bilayer

The experiments in this study are based on continuous lipid bilayers that cover the whole PDMS substrate. The supported lipid bilayer is deposited on top of the stretchable PDMS sheet using vesicle fusion, as described in previous studies.[14] Briefly we prepare small unilamelar vesicles from DOPC phospholipids, mixed with 1 mol% Rh-DPPE fluorescent lipid and suspend them in fusion buffer (10 mM Tris–HCl, 150 mM NaCl, 2 mM CaCl, adjusted with 1 M HCl to pH ≈ 7.5) to a concentration of 0.5 mg lipids per mL. The suspension is deposited on freshly plasma-oxidised PDMS substrate (20 s, 300 W) and incubated for 30 min to achieve vesicle fusion and formation of continuous SLB.

2.4. Imaging and image analysis

The deformation of the PDMS substrate and the response of the lipid bilayer is imaged using an upright confocal microscope (Zeiss LSM 780, 40× magnification) as the stretch progresses.
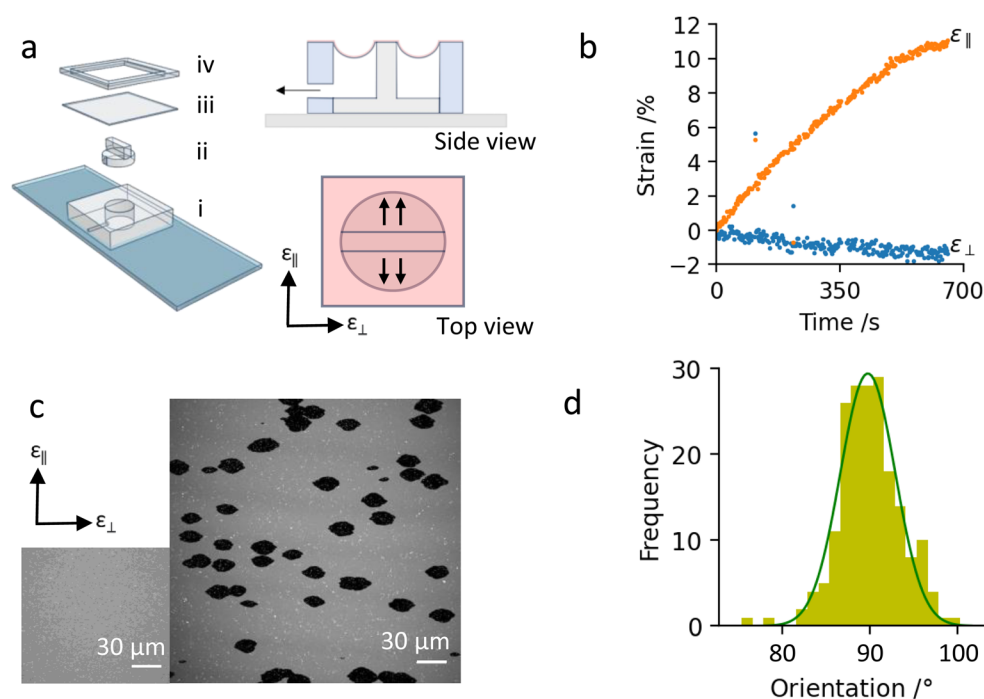

Fig. 1 (a) Custom-made PDMS device for the application of uni-directional stretch to supported lipid bilayers; (i)-PDMS slab, (ii)-acrylic ridge, (iii)-thin PDMS sheet, (iv)-spacer to form a chamber for bilayer deposition. Side and Top views of the PDMS deformation around and on top of the acrylic ridge. (b) Longitudinal ($\varepsilon_\parallel$) and lateral ($\varepsilon_\perp$) membrane strains measured as a function of time across and along the long axes of the acrylic ridge, respectively, as defined in the top-view image in (a). (c) Image of a fluorescently labeled supported bilayer at $\varepsilon_\parallel$ = 11%, with pores appearing as black ellipsoids. The inset shows an area of the same membrane prior to stretching, $\varepsilon_\parallel$ = 0%. Scale bars 30 μm. (d) Orientation of the long axis of the pores with respect to the stretch direction. The plot is based on 191 pores within one sample.

The image time sequences are analysed using FIJI.[18] The images are thresholded to convert the greyscale to binary images allowing pores to be selected out using the Particle Analysis plugin and individually tracked. For each time frame, we extract the membrane strain magnitude, the size of the individual pores, their aspect ratio and the average distance between the pores as explained below. To find the pore aspect ratio, defined as major axis/minor axis, each pore is first fitted to an ellipse and its major and minor axes extracted. The interpore distance is found by averaging the distances between the center of mass of each pore to its three nearest neighbours.

3. Results

3.1. Uniaxial stretch of lipid bilayers

All data in this paper is acquired from the centre of the stretching device, i.e. in the middle of the acrylic support to minimise edge effects. We first characterise the stretch deformation of the PDMS substrate by tracking fluorescent beads embedded in the PDMS sheet as we operate the pump in withdrawal mode (see ESI†). From this we obtain the areal and lateral PDMS strains, defined as $(m - m_0)/m_0$, where m is a measurement of the area between 4 beads or the distance between a pair of beads, respectively. Fig. S1 (ESI†) shows that the PDMS substrate deformation is almost uni-directional. Depending on the target volume of the pump, the PDMS stretches by 10–15% across, and by less than 1% along the length of the acrylic support. Such strain magnitudes are also typical for cell-stretching experiments.[19]

Elsewhere, we have shown that the deformation of the PDMS substrate induces a stretch on the SLB via a frictional coupling.[14,15] The coupling between the PDMS substrate and the lipid bilayer depends on the hydrophobicity of the PDMS substrate, which can be controlled by the duration of plasma exposure prior to vesicle fusion. In these experiments, we use a longer plasma exposure and hydrophilic PDMS substrates onto which the lipid mobility is retained, albeit significantly restricted due to the friction with the substrate.[15]

To characterise the membrane strain due to the PDMS subtrate deformation we track the distance between small membrane defects, usually unfused vesicles. We label the membrane strains along and perpendicular to the directions of the PDMS stretch as longitudinal strain ($\varepsilon_\parallel$) and lateral strain ($\varepsilon_\perp$), respectively (Fig. 1a). Fig. 1b shows thatthe membrane strain closely follow the PDMS strain; $\varepsilon_\parallel$ increases continuously to 10–15% throughout the operation of the pump, while the lateral strain, $\varepsilon_\perp$, decreases slightly by 1–2%.

We note that the strain rate and strain magnitude may differ slightly across devices, even when we apply the same pump settings. This variation is mainly due to differences in the thickness of the PDMS sheet and how it is deposited on the acrylic post. To account for this, we continuously image the bilayers while they are being stretched and compare their response either at a fixed strain magnitude or for a fixed pore size.

3.2. Membrane pore formation under uniaxial stretch

At the start of the stretching experiment, the lipid bialyer appears homogeneously fluorescent (Fig. 1c, inset). As we stretch the PDMS substrate, the membrane opens pores, which can be detected by the absence of fluorescent signal (Fig. 1c, ii). The pores grow only while the substrate is being stretched, and do not change or close while the PDMS strain is kept constant, in agreement to our previous studies[15] (see ESI,† Fig. S2). Most interestingly however, membrane pores have an elliptical shape with the long axis oriented perpendicular to the stretch direction (Fig. 1d). The observation of non-circular pores in fluid lipid membranes is puzzling and suggests that tension equilibration is obstructed. Furthermore, the perpendicular orientation of the pores and their shape resembles the elastic fracture of soft deformable materials.[20] In this paper, we explore this analogy in further details.

3.3. Pore morphology

Fig. 2 shows a representative sample, for which we have analysed pore formation and morphology. Additional samples are added in the ESI.† In general, pores nucleate throughout the stretching process but most of them appear in the first few percent of the stretch, e.g. 70% of the pores in the current sample form in the first 2% membrane strain (Fig. 2b). Pores that open later in the stretch process grow to a smaller final size.

All pores initially appear as circles but as the strain increases, they elongate more rapidly in the direction perpendicular to the applied stretch (Fig. 2a). This can be seen by the increase in their aspect ratio with strain (Fig. 2a and c). Interestingly, pores that open later grow perpendicular to the stretch but very little along it. At the end of the stretch process, there is a clear correlation between the time a pore opens, its size and aspect ratio (Fig. 2d). In general, the later a pore opens, the smaller its final area and the larger its aspect ratio. This dependence is also observed for other samples stretched at different strain rates (ESI,† Fig. S3).

3.4. Effect of strain rate

Next, we examine the effect of substrate strain rate on pore formation. By adjusting the withdrawal rate of the syringe pump, we stretch the membranes at strain rates in the following ranges: slow (10^{-2}% s^{-1}), medium (10^{-1}% s^{-1}) and fast (10^{0}% s^{-1}). All membrane samples are analysed at a strain magnitude of $\varepsilon_\parallel$ = 10%.

Fig. 3a shows images of membrane samples stretched at slow, medium and fast strain rates. The corresponding movies are shown in the ESI,† Movies S1–S3. The membrane strain determined by tracking immobile defects on these bilayers is 12% (slow), 12% (medium) and 15% (fast). The percentage of combined pore area vs. total area is 11.7%, 12.15% and 15.2%, respectively. The close mapping between pore area and membrane strain for all samples indicates that (1) the dominant mechanism for membrane tension release is pore formation, and (2) the extent of membrane rupture, i.e. the total
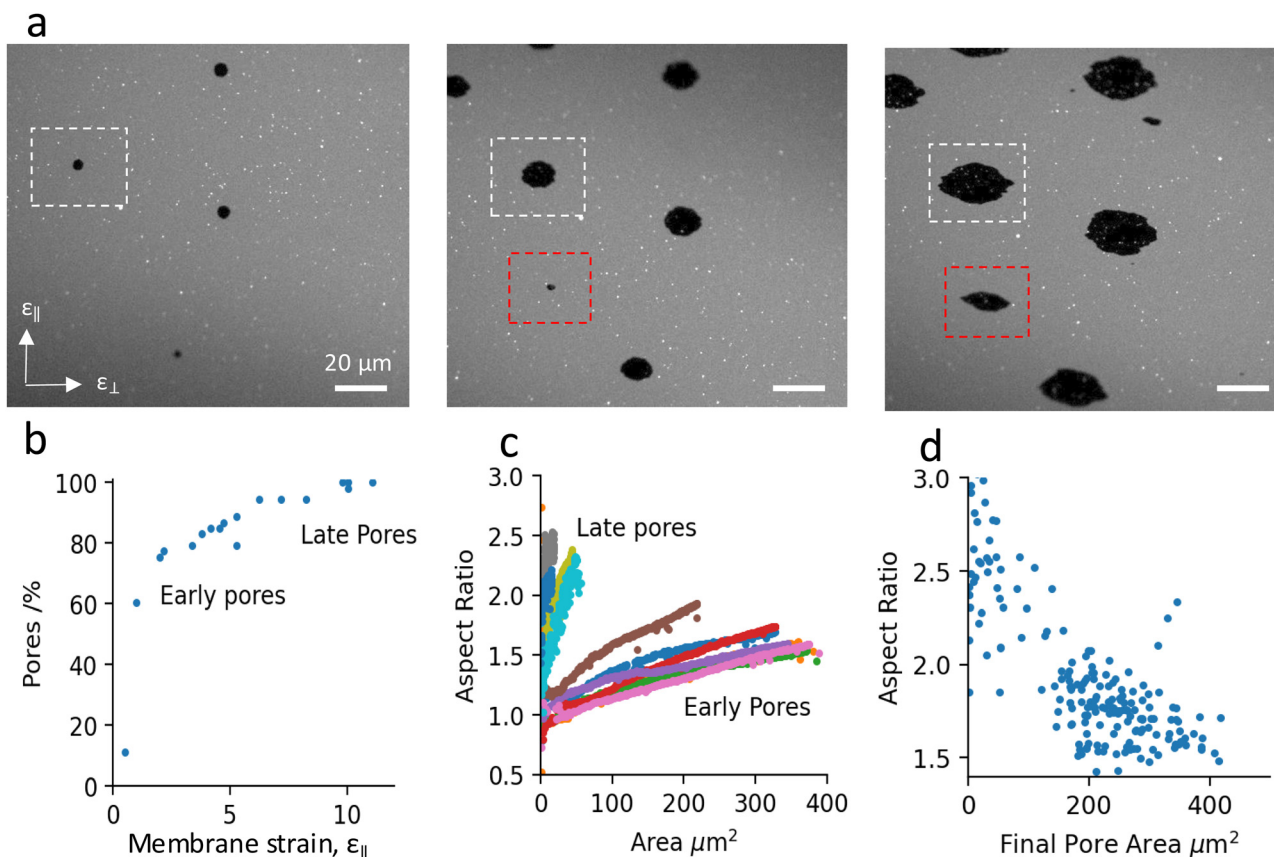
Fig. 2 (a) Confocal images of a supported lipid bilayer under slow uniaxial stretch at 3 different values the membrane longitudinal strain ($\varepsilon_\parallel$ equals 6.5%, 8.8% and 11.1% from left to right). White dashed box shows an example of an early pore and the red box shows an example of a pore that forms later in the stretching process. Plots in (b)−(d) are based on this sample. (b) Percentage of pores (52 pores tracked in total) opened as a function of membrane strain. More than 70% of the pores open up in the first 2% of membrane strain. (c) A plot of aspect ratio *vs.* pore area for 10 selected early and late pores, tracked during the stretch process. (d) A map of the final pore area *vs.* final aspect ratio of all pores within a selected area of the bilayer. The plot is based on 192 pores within the field of view.

fracture area depends only on the stretch magnitude, and not on the strain rate. Strain rate however clearly affects the way SLBs rupture, as seen from the differences in the pore size and the pore number density between the samples on Fig. 3a.

Membranes stretched at slower rates appear to have fewer and much larger pores compared to higher strain rate samples (Fig. 3b). The large variation within and between samples at slow strain rate, can be attributed to the relatively small number of pores, and to the larger effect that late pores have on the average pore size distribution. Despite the large error bars, there is a clear statistical difference between the mean pore sizes as a function of strain rate, verified using 5% significance level *t*-test.

In conjunction with pore area, strain rate affects the inter-pore distance (Fig. 3c). Our experiments show that higher strain rate results in higher density of smaller pores, in agreement with previous experiments on membrane patches subjected to bi-axial stretch.[15] The decrease in inter-pore distance with strain rate can be fitted with a power-law function. Fig. 3c shows two fits to the data: one with a fixed power of −0.5, and another with a free power (see Discussion for more information). The best-fit power law was $y = 7.13x^{-0.335}$, with a standard error of regression of 2.46 μm and the best fit using a function

with a fixed power of −0.5 was $y = 4.02x^{-0.5}$, with a standard error of regression of 2.93 μm.

We then look at whether the strain rate has an effect on the shape of the pores. As discussed previously, the aspect ratio of individual pores depends on the applied strain magnitude, and on when in the stretch process a pore appears (Fig. 2c and d). Therefore to compare pore shape across samples, we select only early pores and measure their aspect ratio for a fixed pore area of 10 μm². This small reference pore size is set by the maximum pore size reached in the high strain rate samples. With these considerations, our results show that the strain rate does not affect the aspect ratio of pores (Fig. 3c) using a 5% significance level *t*-test. In other words, fast strain rates do not lead to more elongated pores. It must be noted however that at this small reference pore size, pore asymmetry is in general small and the measurement uncertainty high, which puts our conclusion under question.

4. Discussion

Lipid bilayers are known to have a high elastic modulus and a small tensile strength, meaning that they resist stretching and can only sustain minimal deformation before rupturing.[5] In
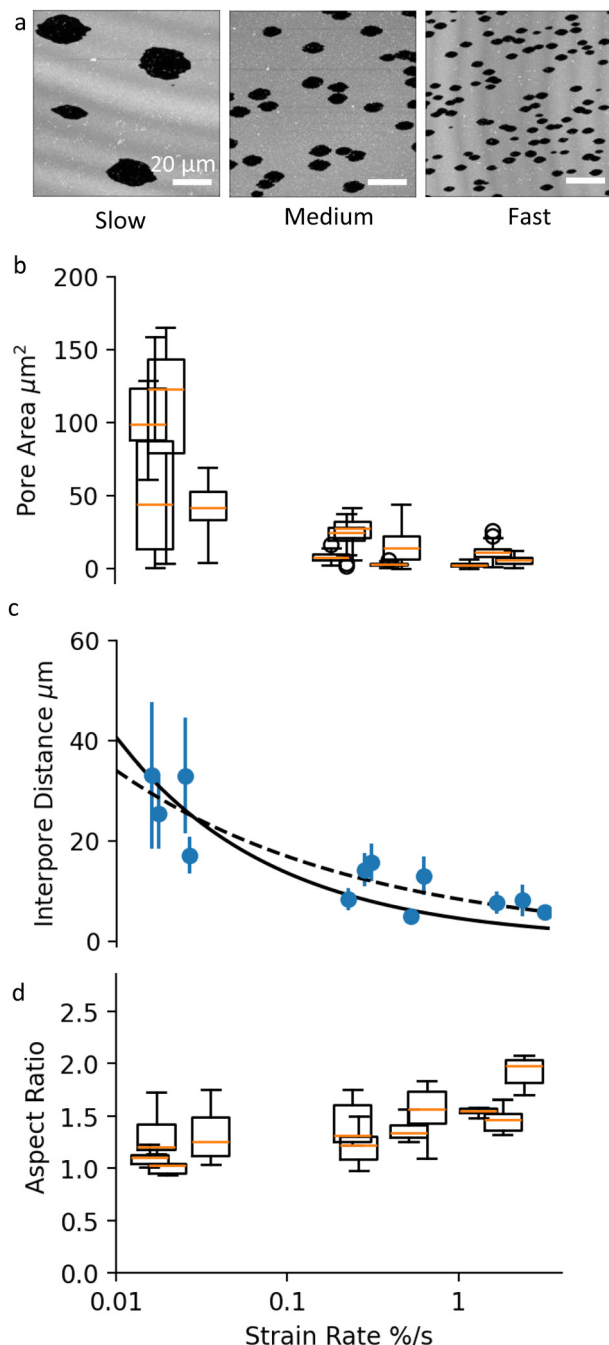
Fig. 3 (a) Images of pores in SLBs at the end of slow, medium and fast uni-axial stretching. Scale bars are 20 μm. (b) Box and whisker plots showing pore size distribution in membrane samples stretched at different rates. Each box and whisker plot represents a different sample. All samples have been analysed at a membrane strain $\varepsilon_\parallel$ = 10%. (c) A plot of the average interpore distance as a function of strain rate. The data points correspond to different samples, analysed at 10% membrane strain. The black solid line shows $y = 7.13x^{-0.335}$, and the black dashed line shows $y = 4.02x^{-0.5}$. (d) Box and whisker plots of the aspect ratio of selected pores in membrane samples stretched at different rates. All pores are analysed when they reach a surface area of 10 μm². No statistical significance between the aspect ratios is detected using a t-test (comparison of means) with 95% confidence interval.

addition, membranes composed of unsaturated lipids, such as DOPC, are in a fluid phase at room temperature, with lipids freely diffusing within the membrane plane. Hence, fluid lipid membranes subjected to stretch can dissipate energy through two mechanisms: (1) membrane rupture and pore formation, where the membrane loses its integrity at discrete locations and releases its stretch-induced tension, and (2) lipid flow along tension gradients.

Tension-driven lipid flows in supported lipid bilayers and in biological membranes underlined by the cell cytoskeleton are shown to be opposed both by viscous and friction forces.[8,11] The ratio between the viscosity of the bilayer (μ) and the membrane sliding friction with the substrate (ζ) defines a characteristic length-scale, $L = \sqrt{\mu/\zeta}$, which indicates the relative significance of these forces in lipid flows. Large scale flows on length scale exceeding L, are limited by the friction of the membrane with the supporting substrate, whereas local lipid rearrangement is governed by viscous forces. Taking literature values for $\mu \approx 1 \times 10^{-10}$ Pa m s (ref. 21) and $\zeta \approx 1 \times 10^{8}$ Pa s m^{-1} (ref. 15,22) we obtain a value of L in the range of a few tens of nanometers, which falls within the length-scale relevant for pore formation. We therefore expect that small-scale lipid rearrangement in the vicinity of growing pores will be governed mostly by viscous forces, whereas the larger scale lipid dynamics, which sets the pore size and inter-pore distance will predominantly depend on the membrane-substrate sliding friction.

In our experiments, we apply gradually increasing uniaxial strain to lipid bilayers by stretching the underlying membrane support. As a result, the tension in the bilayer increases and once it reaches a critical value (usually at 1–2% strain), the bilayer opens pores to release its tension (Fig. 2a and b). The growth of pores with increasing membrane strain is opposed by viscous and frictional drag forces, which lead to further accumulation of membrane tension and opening of new ('late') pores (Fig. 2b). In contrast to vesicle systems, pores in SLBs can have irregular shape[10,11] and can stay open for a long time[15] (ESI,† Fig. S2), even if the membrane tension is low. This is due to the strong frictional coupling between the membrane and the substrate, which effectively counteracts the edge tension acting to minimise the pore perimeter. Previous studies have presented scaling arguments that support these observations.[10,11]

The density of pores on the SLB, and the inter-pore distance respectively, R, depend on the rates of tension increase and tension dissipation as $R \sim \sqrt{K/\zeta\dot{\varepsilon}}$, where K [J m^{-2}] is the membrane elastic modulus, ζ is the friction coefficient, and $\dot{\varepsilon}$ [s^{-1}] is the applied strain rate.[8,15] R can also be understood as the distance over which a pore reduces the membrane tension in its vicinity. Higher strain rates correspond to shorter times for lipid relaxational flow, hence shorter R. As a result, SLBs stretched at higher rates exhibit a higher density of smaller pores. Fig. 3c confirms the expected square-root dependence between inter-pore distance and strain rate. The deviation of the perfect fit from the predicted powerlaw of $-\frac{1}{2}$ can be ascribed to a non-homogeneous pore distribution (Fig. 3a), possibly arising from pre-existing membrane and substrate defects that lower the threshold for pore nucleation.

All pores initially have a circular shape but quickly transform into ellipsoids as they grow faster in the direction perpendicular to the applied stretch (Fig. 2a). Although such behavior has not been observed, nor predicted[16,17] for fluid bilayers, it has been well characterised in the context of elastic fracture mechanics in solid materials. Defects and cracks in solid materials induce inhomogeneities in the stress field, with stress concentrating at the crack tip. Stress concentration may lead to spontaneous crack propagation and material failure in solids at much smaller tensile loads.[23] Similarly, tension in the bilayer is amplified at the lateral sides of the pores (Fig. 4a) causing them to grow into ellipsoids oriented perpendicular to the strain direction.

A close examination of the membrane pore profile reveals a combination of responses and a complex membrane rheology. Most membrane pores, especially the early ones, exhibit a wide ellipsoidal profile (relatively small aspect ratio), characteristic for the fracture of soft elastic solids, such as rubber or gels.[20,24,25] We suggest that the apparent softness of the otherwise inextensible membrane stems from tension relaxational flows within the membrane plane. Such flows have been previously visualised in isolated SLB patches that simultaneously slide and form pores in response to substrate deformation.[15] Tracking the edge of the patches under uniaxial stretch reveals that they elongate in the direction of the stretch, at the expense of an incoming flow of lipids from the sides (Fig. 4b and ESI,† Movie S4). But the membrane pores are not completely ellipsoidal. At the tip of the pores, we see a much narrower crack profile that characterises the fracture behaviour of stiff materials (Fig. 4c and d). Such pore profiles, called 'visco-elastic trumpets'[20] have been described in visco-elastic solids, and reflect different strain rates and different material responses around the crack. At the sides of the pore (facing the stretch direction), the membrane responds as a soft deformable material with effectively lower elastic modulus, K^* due to creep flows. At the tip however, the speed of the pore propagation and the strain rate are highest, and the membrane behaves elastically with its high elastic modulus (K). Interestingly, pores that open later in the stretch process have a much narrower opening profile and a higher aspect ratio (Fig. 2c and d). This suggests that the capacity of the SLB for large-scale relaxational flow may be exhausted as the stretch progresses.

Our data do not show a significant correlation between the mean aspect ratio of the pores and the rate of stretching applied to the membrane (Fig. 3d). Moreover, we observe trumpet-shaped pores at all strain rates (Fig. 3a). Previous analysis of cracks in visco-elastic materials has argued that trumpet shapes appear at rates of crack propagation comparable to the relaxation rate of the visco-elastic material.[20] In our membrane experiments however, a fast strain rate becomes compensated by a larger density of pores and not by faster pore growth rate.

5. Summary and outlook

In this work we describe the response of supported lipid bilayers to uniaxial stretch. We observe ellipsoidal pores that grow perpendicularly to the stretch direction, similarly to tearing of deformable elastic materials under tensile loading. The trumpet-like pore shape, characteristic of visco-elastic materials indicates a distribution of strain rates around the pore and a rate-dependent membrane behaviour, ranging from global relaxational lipid creep flow to solid tearing at the tip of the pores. Our work implies for a first time a close analogy between the fracture mechanisms of supported lipid membranes and of deformable elastic materials, such as gels.[20] The key parameter here appears to be the membrane-substrate friction, which obstructs the lipid dynamics and the membrane tension equilibration, in agreement with previous studies on SLB systems.[11–13] Going forward, we need a theoretical model that links quantitatively the material properties of the lipid membrane and its tension distribution under different loading conditions to its fracture behaviour.

Our results on the gel-like fracture of supported lipid membranes agree with previous research showing that cell membranes behave more like a semi-solid gel than a viscous fluid.[8,9] These studies reported a very slow tension equilibration on the cell surface, caused by membrane-cytoskeleton attachments hindering the lipid flow. In relation to cell membrane rupture and healing, our study implies that the
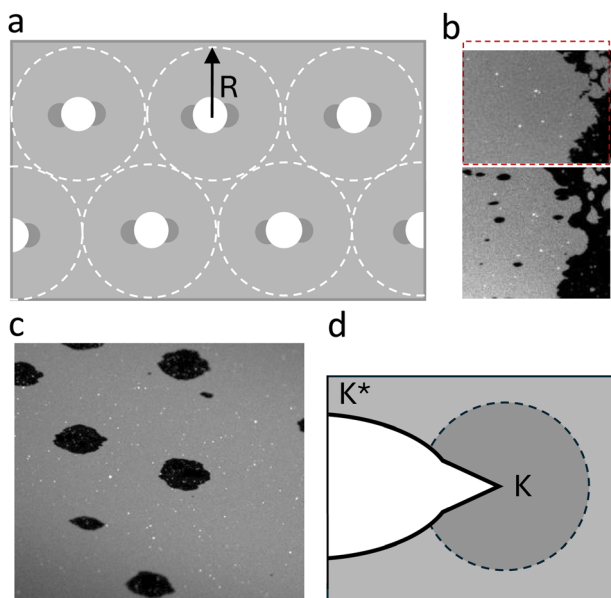

Fig. 4 (a) Schematic drawing of the tension distribution in the membrane, with dark shades of grey indicating stress concentration at the tip of the pores. R corresponds to the tension diffusion length. (b) Microscopic images of a supported lipid bilayer patch made of DOPC lipids before and after the stretch. Full video in ESI.† The red box shows the dimensions of the sample achieved after the stretch. (c) Image of membrane pores with viscoelastic trumpet shapes. Scale bar is 20 µm. (d) Viscoelastic trumpet structure characteristic of the failure behaviour of materials with rate dependent properties. The tip of the crack is characterised by large tension, high elastic modulus (K), and a sharp crack propagation. Away from the pore tip, membrane behaves as a deformable material with lower elastic modulus, K^*.

shape of the pores in cells will strongly depend on the local distribution of the membrane tensile stress, and that edge tension will have little effect on the pore shape and its closure. It remains to be studied whether the irregularity of pore perimeter and the variation in the pore edge curvature may control the pore closure process by facilitating protein and lipid recruitment.[1,2]

Author contributions

Both authors designed the experiments, analysed the data and wrote the paper. RG built and optimised the stretching setup and performed the experiments.

Data availability

Data for this article, including raw images and data analysis is available at Durham University research data repository with identifier **https://doi.org/10.15128/r1wm117p070**.

Conflicts of interest

There are no conflicts to declare.

Acknowledgements

Notes and references

1 C. Dias and J. Nylandsted, *Cell Discovery*, 2021, **7**, 4.
2 D. A. Ammendolia, W. M. Bement and J. H. Brumell, *BMC Biol.*, 2021, **19**, 71.
3 M. S. Clarke, R. W. Caldwell, H. Chiao, K. Miyake and P. L. McNeil, *Circ. Res.*, 1995, **76**, 927–934.
4 O. Sandre, L. Moreaux and F. Brochard-Wyart, *Proc. Natl. Acad. Sci. U. S. A.*, 1999, **96**, 10591–10596.
5 D. Needham and R. S. Nunn, *Biophys. J.*, 1990, **58**, 997–1009.
6 E. Evans, V. Heinrich, F. Ludwig and W. Rawicz, *Biophys. J.*, 2003, **85**, 2342–2350.
7 D. V. Zhelev and D. Needham, *Biochim. Biophys. Acta, Biomembr.*, 1993, **1147**, 89–104.
8 Z. Shi, Z. T. Graber, T. Baumgart, H. A. Stone and A. E. Cohen, *Cell*, 2018, **175**, 1769–1779.e13.
9 A. E. Cohen and Z. Shi, *BioEssays*, 2020, **42**, 1900142.
10 I. Gözen, P. Dommersnes, I. Czolkos, A. Jesorka and T. Lobovkina, *Nat. Mater.*, 2010, **9**, 908–912.
11 I. Gozen and P. Dommersnes, *Eur. Phys. J.: Spec. Top.*, 2014, **223**, 1813–1829.
12 M. Taylor, I. Gözen, S. Patel, A. Jesorka and K. Bertoldi, *PLoS One*, 2016, 1–14.
13 O. Shindell, N. Mica, K. H. Cheng, E. Wang and V. D. Gordon, *Langmuir*, 2018, **34**, 4673–4680.
14 M. Staykova, D. P. Holmes, C. Read and H. A. Stone, *Proc. Natl. Acad. Sci.*, 2011, **108**, 9084–9088.
15 L. Stubbington, M. Arroyo and M. Staykova, *Soft Matter*, 2017, **13**, 181–186.
16 L. Zhang, Z. Zhang, J. Jasa, D. Li, R. O. Cleveland, M. Negahban and A. Jérusalem, *Sci. Rep.*, 2017, **7**, 8316.
17 Z.-J. Wang and D. Frenkel, *J. Chem. Phys.*, 2005, **123**, 154701.
18 J. Schindelin, I. Arganda-Carreras and E. E. A. Frise, *Nat. Methods*, 2012, 676–682.
19 I. Constantinou and E. E. Bastounis, *Trends Biotechnol.*, 2023, **41**, 939–950.
20 R. Long, C.-Y. Hui, J. P. Gong and E. Bouchbinder, *Annu. Rev. Condens. Matter Phys.*, 2020, **12**, 71–94.
21 H. A. Faizi, R. Dimova and P. M. Vlahovska, *Biophys. J.*, 2022, **121**, 910–918.
22 P. Jönsson, J. P. Beech, J. O. Tegenfeldt and F. Höök, *Langmuir*, 2009, **25**, 6279–6286.
23 J. F. Knott, *Fundamentals of fracture mechanics*, Butterworth, London, 1973.
24 C.-Y. Hui, J. A, S. J. Bennison and J. D. Londono, *Proc. R. Soc. London, Ser. A*, 2003, **459**, 1489–1516.
25 C. Creton and M. Ciccotti, *Reports on progress in physics. Physical Society, Great Britain*, 2016, **79**, 046601.